JOURNAL OF MATERIALS RESEARCH AND TECHNOLOGY 2020;**9(6)**:14754–14770

Available online at www.sciencedirect.com

jmr&t
Journal of Materials Research and Technology

journal homepage: www.elsevier.com/locate/jmrt

Original Article

Surface chemistry, film morphology, local electrochemical behavior and cytotoxic response of anodized AZ31B magnesium alloy

Leandro Antonio de Oliveira [a,*], *Rejane Maria Pereira da Silva* [b], *Andrea Cecilia Dorion Rodas* [a], *Ricardo M. Souto* [c], *Renato Altobelli Antunes* [a]

[a] *Centro de Engenharia, Modelagem e Ciências Sociais Aplicadas (CECS), Universidade Federal do ABC (UFABC), Santo André, 09210-580, Brazil*
[b] *Instituto de Pesquisas Energéticas e Nucleares, IPEN/CNEN, Av. Prof. Lineu Prestes, 2242, São Paulo, Brazil*
[c] *Department of Chemistry, University of La Laguna, P.O. Box 456, La Laguna, Tenerife, 38200, Spain*

ARTICLE INFO

Article history:
Received 10 July 2020
Accepted 21 October 2020
Available online 27 October 2020

Keywords:
AZ31B magnesium alloy
Anodizing pretreatment
Corrosion resistance
Cytotoxicity
SECM
SKP

ABSTRACT

This work investigates the effect of current density on the surface chemistry, film morphology, cytotoxic response, global and local electrochemical behaviors of AZ31B alloy anodized in 1.0 M NaOH + 0.5 M Na_2SiO_3 solution. Three different current densities, namely 5, 10 and 20 mA cm^{-2} were tested. The surface morphology and thickness of the anodized layers were examined by scanning electron microscopy. The surface chemical states were assessed by X-ray photoelectron spectroscopy. The corrosion resistance was evaluated in phosphate-buffered saline (PBS) based on electrochemical impedance spectroscopy and potentiodynamic polarization measurements. The use of scanning probe techniques with physicochemical resolution, the scanning electrochemical microscopy (SECM) and the scanning Kelvin probe (SKP), allowed the best corrosion behavior to be assigned to the sample anodized using a current density of 20 mA cm^{-2}. Altogether, these methods allowed to establish that the anodizing current density imposed to the magnesium alloy had a major effect on the morphology and composition of the surface layers, and produced changes in their electrochemical behavior. *In vitro* cytotoxicity tests using the MTS assay demonstrated that the good biocompatibility of the AZ31B magnesium alloy was not damaged by the surface layers formed during the anodization treatment.

---

[*] *Corresponding author.*
E-mail address: leandro.oliveira@ufabc.edu.br (L.A. de Oliveira).

https://doi.org/10.1016/j.jmrt.2020.10.063

1. Introduction

Magnesium alloys have attracted considerable interest as potential candidates for bioresorbable implant applications. Since they biodegrade via corrosion reactions in the human body, a second surgery is not needed to remove them after the healing process is completed, which is expensive for the health care system and dangerous for the patient [1–8].

However, the main shortcoming of using these materials as temporary implant devices is their high degradation rates, which are accompanied by the evolution of hydrogen gas (approximately 1 L per gram of corroded Mg [9]) and lead to the formation of hydrogen gas cavities in tissues [5,10,11]). Additionally, magnesium alloys suffer severe local corrosion attack, implying in premature loss of mechanical integrity, thus hindering their further clinical use, especially in orthopaedical and cardiac applications [4,12–15]. Fortunately, there are several possibilities of controlling the corrosion rate of magnesium-based materials, such as alloying, mechanical pre-processing and surface modifications [1,16,17]. Anodization is an electrolytic oxidation process in which the surface of the metal is converted to an oxide film having desirable corrosion protection and functional properties [18–23]. The treatment promotes an increase in the film thickness, hardness, wear resistance, and biocompatibility with respect to the bare metal [3,20]. The anodizing conditions have a major influence on the properties of the anodized film. Several investigations have shown the effects of electrolyte composition, treatment duration, electrical parameters, and post- and pre-treatments on the composition and morphology of the anodic films [18,24–30]. Thus, the search for an optimized set of processing parameters, which interact with each other, is necessary to obtain a film with desired functionalities.

Although conventional electrochemical tests are usually employed to investigate the corrosion activity of materials, they only provide an averaging characterization of the corroding surface. Conversely, scanning probe electrochemical techniques exhibit spatial resolution, and they are becoming increasingly applied to these studies since they allow a comprehensive understanding of the local corrosion processes occurring at specific electrochemically active sites. Among them, scanning electrochemical microscopy (SECM) and scanning Kelvin probe (SKP) have been successfully used to characterize localized corrosion processes of different metallic materials, such as aluminum alloys [31–33] and steels [34–36]. The degradation of magnesium alloys at a microscopic level is also becoming investigated using these methods [37–42]. Notwithstanding, the assessment of local corrosion spots of anodized layers produced on magnesium alloys by combining SECM and SKP are scarcely reported in the current literature.

In this study, we investigate the potentiality of anodization to control the dissolution rate of magnesium alloy in a simulated biological environment. The main focus is to study the correlation between film morphology, the chemical composition of the anodized layers, cytotoxic response and their global and local electrochemical behaviors. The use of SECM and SKP to probe the local corrosion sites developed on anodized layers of magnesium alloys and the correlation between this information with the surface chemistry and global electrochemical response is rarely employed in the current literature.

2. Material and methods

2.1. *Material and sample preparation*

Hot rolled AZ31B magnesium alloy sheet (composition in wt.%: Al 2.54%, Zn 1.08%, Mn 0.38% and Mg balance), supplied by Xi'an Yuechen Metal Products Co. Ltd. (Xi'an, Shaanxi, China), was used as the substrate for the anodization process. Rectangular pieces were cut from the as-received sheet using a cut-off saw, obtaining dimensions of 10 mm × 10 mm × 3.5 mm. The specimens were connected to a copper wire at the rear side, and then they were embedded in epoxy resin mounted in a PVC holder, leaving an average area of 1 cm^2 as the working surface. The surfaces were sequentially ground using waterproof silicon carbide paper (from #220 to #2400 grit size), polished using diamond paste slurry (diameter 1 μm), and cleaned using deionized water and ethanol, being subsequently dried in a warm air stream provided by a conventional heat gun.

2.2. *Anodizing treatment*

The anodization process was carried out with a high voltage DC power supply (MP5003D, 50–500 V, 0–3 A; Shenzhen, Guangdong, China). The anodization treatments were performed in an aqueous solution consisting of a mixture of 1.0 M NaOH and 0.5 M Na_2SiO_3. The AZ31B magnesium alloy was connected as the anode, while the stainless steel container was used as the cathode. The anodizing treatment was carried out at three different constant current densities, namely 5 mA cm^{-2}, 10 mA cm^{-2} and 20 mA cm^{-2}, for 5 min at room temperature. Finally, the anodized samples were rinsed with deionized water and let naturally dry.

2.3. *Film characterization*

2.3.1. *Morphology, roughness and chemical composition*

The surface and cross-section morphologies were examined using scanning electron microscopy (SEM, JSM-6010LA, JEOL, Tokyo, Japan). Confocal laser scanning microscopy (CLSM, LEXT OLS4100, Olympus, Tokyo, Japan) was used to determine the surface roughness. Roughness values were quantified in terms of the average roughness, R_a.

The crystalline character of the anodized layers was assessed by grazing angle X-ray diffraction (XRD) in a Bruker AXS, D8 Discover diffractometer, using Mo-kα radiation (0.071 nm). The step size was 0.02° at a scan rate 4°.min^{-1}. The 2θ range was from 5 to 40°. .XPS analyses were performed to investigate the chemical composition of the anodized films. The XPS spectra were acquired using a Thermo Fisher Scientific K-$Alpha^+$ spectrometer with a monochromated Al K-α X-ray source (Waltham, MA, USA). The energy scale was calibrated with respect to the adventitious C 1s peak at 284.8 eV. High resolution spectra for the Mg 2p, Si 2p and O 1s regions were obtained to assess the surface chemical states. The spectra were deconvoluted by curve-fitting using the *Smart* baseline for background subtraction in the Avantage™ software (Thermo Fisher Scientific, Waltham, MA, USA).

2.3.2. *Electrochemical characterization*

2.3.2.1. *Conventional electrochemical tests*. Electrochemical measurements were assessed using a potentiostat/galvanostat (M101, Autolab) in a conventional three-electrode cell configuration. The test cell consisted of Ag/AgCl (3 M, KCl) as the reference, a platinum wire as the counter electrode, and the investigated AZ31B alloy as the working electrode. The tests were conducted in phosphate-buffered saline (PBS) solution, which contains: 0.355 g L^{-1} $NaH_2PO_4 \cdot H_2O$, 8.2 g L^{-1} NaCl, 0.105 g L^{-1} Na_2HPO_4 (anhydrous). The solution was prepared with deionized water and analytical grade reagents. Initially, the open circuit potential (OCP) was monitored for 1 h. Subsequently, the samples were subjected to electrochemical impedance spectroscopy (EIS) at the OCP using a 10 mV AC voltage amplitude in the frequency range between 100 kHz and 0.1 Hz. Right after recording the impedance spectrum, potentiodynamic polarization tests were carried out in a potential range extending from −0.50 V vs. OCP to 0 V vs. Ag/AgCl/(3 M, KCl), at a scanning rate of 1 mV s^{-1}. Experiments were performed in triplicate.

The porosity degree of the anodized AZ31B samples was estimated using an electrochemical method based on the measurement of polarization resistance (Rp) values from the potentiodynamic curves. This method consists in determining the variation of the corrosion potential ($\Delta E_{corr} = E_{corr,\ substrate} - E_{corr,\ substrate+coating}$) caused by the presence of the anodized layer and from individual measurements of the polarization resistance (R_p) of the polished and anodized AZ31B using Eq. (1) [43,44]:

$$P = \left(\frac{R_{p,s}}{R_p}\right) \times 10^{\frac{|\Delta E_{corr}|}{b_a}} \qquad (1)$$

where $R_{p,s}$ denotes the polarization resistance of the polished substrate and R_p is the polarization resistance of the anodized substrate, while b_a is the anodic Tafel slope of the bare substrate. $R_{p,s}$ and b_a are determined from separate measurements of the polished substrate.

2.3.2.2. *Scanning probe techniques*. Spatially-resolved measurements were made at room temperature and with the substrate at the open circuit potential (unbiased). The AZ31B alloy was cut into strips and then embedded in epoxy resin to expose upwards a working area of approximately 0.25 cm^2.

A scanning electrochemical microscopy (SECM) built by Sensolytics (GmbH Bochum, Germany) was used to evaluate the local corrosion process on the AZ31B alloy surface immersed in PBS. A three electrode configuration was employed, with a 25 μm Pt disk ultra-microelectrode (UME) tip as the working electrode, Pt as the auxiliary electrode, and an Ag/AgCl/(3 M, KCl) as reference electrode to complete the small electrochemical cell. SECM experiments were performed at selected heights of the tip above the investigated surface. The operating height was set after recording Z-approach curves, with the tip adjusted to 10 μm above the surface. SECM measurements were performed using the surface generation/tip collection (SG/TC) mode by monitoring the H_2 evolution accompanying the corrosion process of the magnesium alloy. This species was monitored by setting the potential of the UME probe at 0.0 V vs. Ag/AgCl (3 M, KCl) for the reoxidation of hydrogen.

SECM maps in constant height mode were obtained by scanning the UME tip in the X–Y plane and recording the tip current as a function of its location. The maps were recorded after 30 min immersion of the corresponding AZ31B sample in PBS solution. A randomly chosen area of 400 μm × 200 μm was examined.

Scanning Kelvin Probe (SKP) measures the Volta potential difference between the working electrode and the probe, which vibrates above the sample surface in air. The SKP experiments were performed in a VersaScan electrochemical workstation (AMETEK, Devon–Berwyn, PA, USA) at room temperature in air. The distance between the probe tip and the specimen surface was maintained at 100 μm ± 10 μm throughout the tests, thus avoiding potential fluctuation stemming from the change in distance. Scanning steps of 200 μm and 500 μm were used for *X* and Y, respectively. The scans were acquired over a 3.6 mm × 6.0 mm region, thus scanning the complete magnesium alloy strip.

2.3.3. In-vitro *biocompatibility*

NIH-3T3 (murine fibroblasts) cells were employed for cytotoxicity analysis. Cells were maintained on a regular feeding regime in a cell culture incubator at 37 °C/5% CO_2/95% air atmosphere for 72 h. The culture media was DMEM (Dulbecco's Modified Eagle Medium) supplemented with 10% fetal bovine serum and 1% antibiotic/antimycotic solution. The samples were immersed in the cellular medium at final concentration of 6 cm^2/mL. The cell viability was evaluated using the Methyl Tetrazolium (MTS) assay in 96 well plates. Liquid extracts were added into wells containing 3T3/NIH cells in culture medium. The MTS assay was then added and the cultures were reincubated for further 2 h (37 °C/5% CO_2). Next, the cultures were removed from the incubator and the absorbance was measured at a wavelength of 490 nm. A sterile medium was used as a control, and the cells were assumed to have metabolic activities of 100% in normal medium culture. The cell viability was calculated using Eq. (2):

$$\text{Cell viability} = \frac{OD_{Sample}}{OD_{Control}} \times 100 \qquad (2)$$

where OD_{Sample} is the optical density of the sample, and $OD_{control}$ is the optical density of the control.

3. Results

3.1. *Morphological and topographical aspects of the anodized layers*

SEM micrographs of the top surfaces of the AZ31B alloy in the as-polished and anodized conditions are shown in Fig. 1. The as-polished surface presents small white-colored precipitates whose composition is mainly comprised of Al and Mn as confirmed by EDS analysis (cf. Fig. 2). Similar findings were reported by other authors [45]. A greatly modified

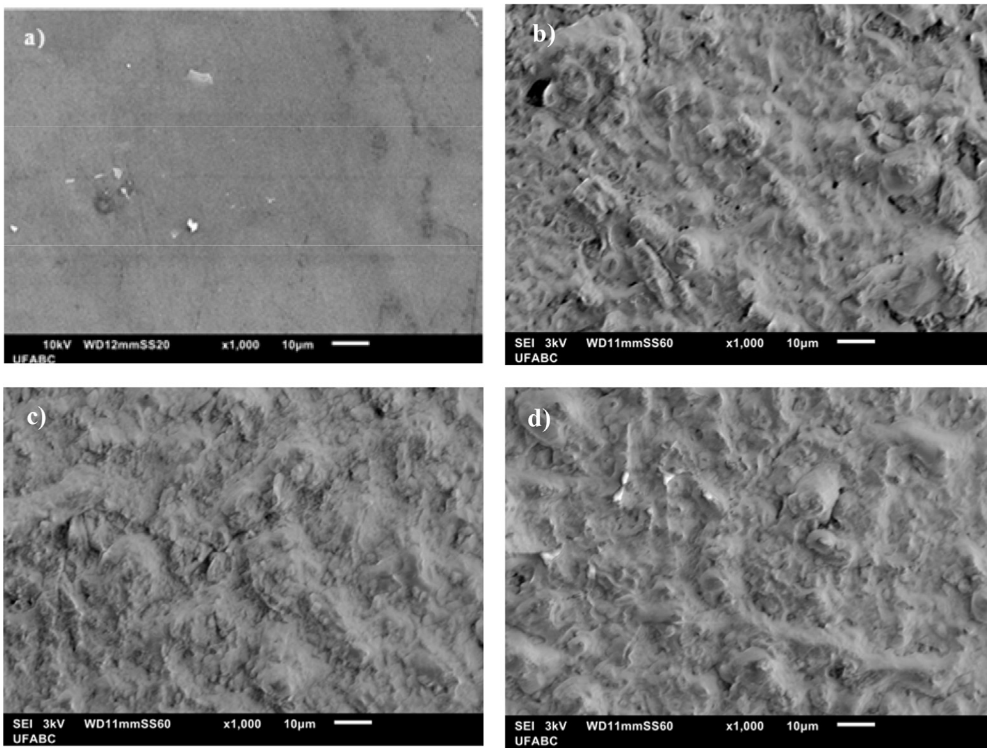

Fig. 1 – SEM images of the top surfaces of AZ31B alloy as polished (a) and after electrochemical anodization in 1.0 M NaOH + 0.5 M Na_2SiO_3 solution at constant current density values: (b) 5, (c) 10, and (d) 20 mA cm^{-2}.

surface topography results from the anodization procedure applied to the AZ31B alloy. The anodized layer completely covered the substrate independently of the current density applied. The compactness of the surface film, in turn, was affected by this parameter. As seen in Fig. 1b, the anodization film formed over the sample treated with 5 mA cm^{-2} current density was discontinuously distributed throughout the surface, showing several cracks and carved regions. These features were less pronounced when the anodizing current was increased to 10 mA cm^{-2} (see Fig. 1c). Finally, the surface produced at 20 mA cm^{-2} exhibited the most compact appearance as shown in Fig. 1d, although some cracks are still present. Therefore, the anodized layer became more compact as the current density was raised from 5 to 20 mA cm^{-2}. Similar observations were reported by Chai et al. [26] for AZ91 magnesium alloy although operating at somewhat higher current densities than the values employed in our work.

As the thickness of the anodized film may greatly affect its corrosion protection ability, cross-sections of the anodized samples were examined by SEM (Fig. 3). The film obtained at 5 mA cm^{-2} was the thinnest one (see Fig. 3a), extending approximately 1 μm. The increase of the anodizing current density to 10 mA cm^{-2} resulted in an approximately ten-fold increase of the thickness of the resulting layer according to Fig. 3b. The increasing trend was not kept, though, when the current density was raised to 20 mA cm^{-2} (Fig. 3c). Notwithstanding, the interface between the substrate and the anodic layer became more homogeneous than for the film produced at 10 mA cm^{-2} which can be beneficial to its barrier properties against electrolyte penetration.

Further evaluation of the topographical features of the anodized layers was carried out by confocal laser scanning microscopy (CLSM). The average roughness (R_a) was, therefore, determined from CLSM micrographs shown in Fig. 4 for the systems under investigation, and they are listed in Table 1 In addition, representative transverse profiles of scanned lines taken across the sample surface are also given in Fig. 4. The anodized films presented an marked increase of the R_a values with respect to the as polished condition. But the variation of the anodizing current density did not significantly affect the average roughness of the anodic film, since the R_a values shown in Table 1 are very similar for all the anodized layers within experimental error, although there was a major increase in the film thickness when the current density was raised from 5 mA cm^{-2} to 10 mA cm^{-2}. This observation apparently contradicts the report by El Mahallawy et al. [46] that the surface roughness of the anodized layers formed on the AZ91 magnesium alloy increased with the current density and the thickness of the anodic film. Nevertheless, it must be noticed that higher current densities were employed in that work and were operated at a higher temperature, leading to the development of thicker surface layers displaying higher R_a values on AZ91 than in our case. For the sake of comparison, for the film produced using the same current density and anodization time in the most similar electrolyte (although containing rather high concentrations of sodium carbonate and sodium tetraborate leading to a less alkaline environment), they reported a surface layer of ca. 20 μm thickness and an average roughness value $R_a \approx 16$ μm, almost 5 times higher than the findings of this work. In addition, the resulting surface roughness was also greatly affected by the occurrence of

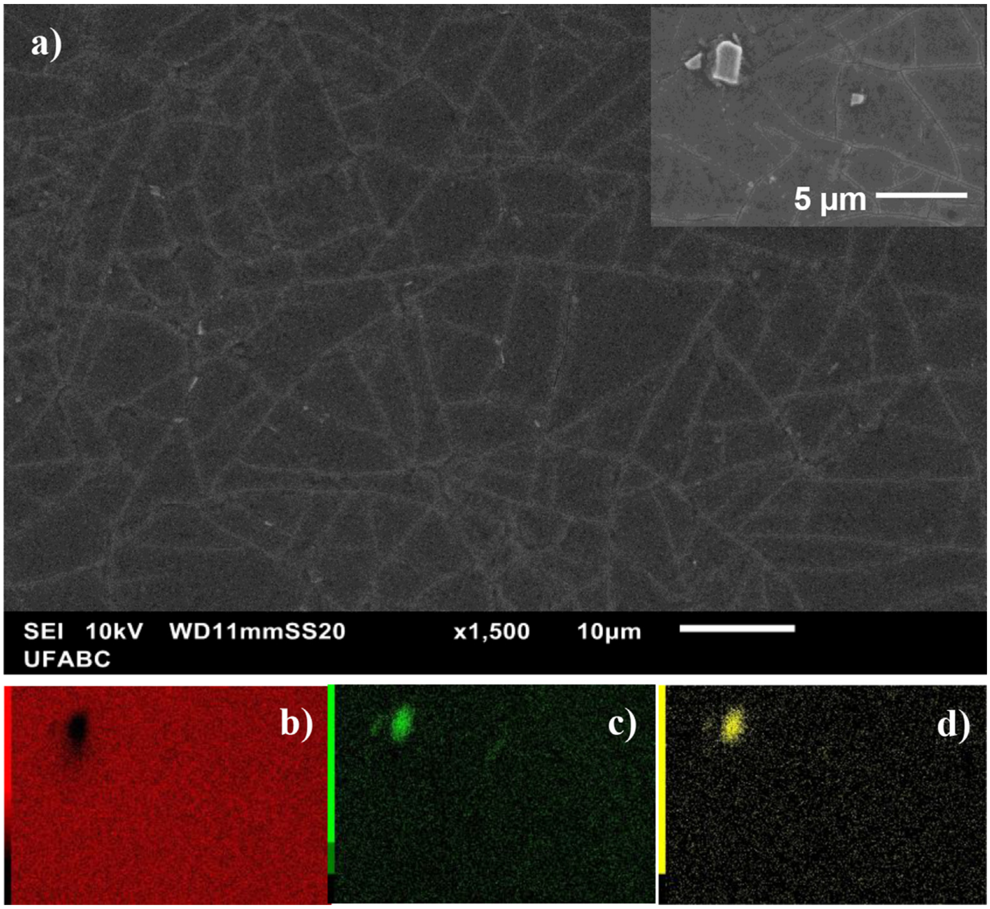

Fig. 2 – SEM-EDS characterization of the AZ31B alloy: (a) SEM images of the microstructure in different scales, and EDS elemental maps of: (b) Mg, (c) Al, and (d) Mn.

pores and cracks in the anodic films formed on AZ91 in that work [46], whereas the thinner films produced on the AZ31B magnesium alloy under less vigorous anodizing conditions were more compact and could be regarded practically free of cracks and macroscopic pores.

3.2. *XRD and XPS characterization*

XRD patterns of the as-polished and 10 mA cm^{-2} samples are shown in Fig. 5. The XRD patterns of the other anodized samples are now shown, as they are very similar to that of the 10 mA cm^{-2} sample. Peak identification was based on ICDD database (card number 00-035-0821). The patterns are quite similar for the as-polished and anodized samples. Only magnesium peaks were identified. These results suggest that the anodized layers have an amorphous character. Chai et al. [26] have also reported the amorphous character of anodized films formed on the AZ31 magnesium alloy. The rapid solidifications of molten particles formed during sparking formation in the anodization process. Our results point to the same direction.

XPS survey spectra of the as-polished and the anodized AZ31B alloy samples are shown in Fig. 6. The main elements present in the anodized films were Mg, Si, Na and O. The presence of Al was detected only in the as polished sample because it is part of the naturally formed oxide film on the surface of the AZ31B alloy. Si and Na were not detected in the as polished alloy, since these elements were included during exposure to the anodizing electrolyte. Detailed information about the surface chemical states of the anodized layers was achieved by acquiring XPS high resolution spectra for the Mg 1s, Si 2p and O 1s regions.

The Mg1s core level spectrum for the sample anodized at 20 mA cm^{-2} is shown in Fig. 7. Very similar spectra were recorded for the samples obtained at 5 mA cm^{-2} and 10 mA cm^{-2}, and they are not shown here. The spectrum was deconvoluted into two components, one at 1303.3 eV that is ascribed to $Mg(OH)_2$ [47], whereas the component with the highest binding energy (1304.2 eV) is assigned to Mg_2SiO_4 [48]. It is observed that magnesium hydroxide is the dominant species, although the anodic film consists of a mixture of $Mg(OH)_2$ and Mg_2SiO_4 independently of the current density employed during the anodization procedure. The formation of these species during anodization of magnesium alloys is in accordance with the literature, and it is related to the following reactions [49]:

$$Mg^{2+} + 2e^{-} \rightarrow Mg(OH)_2 \quad (3)$$

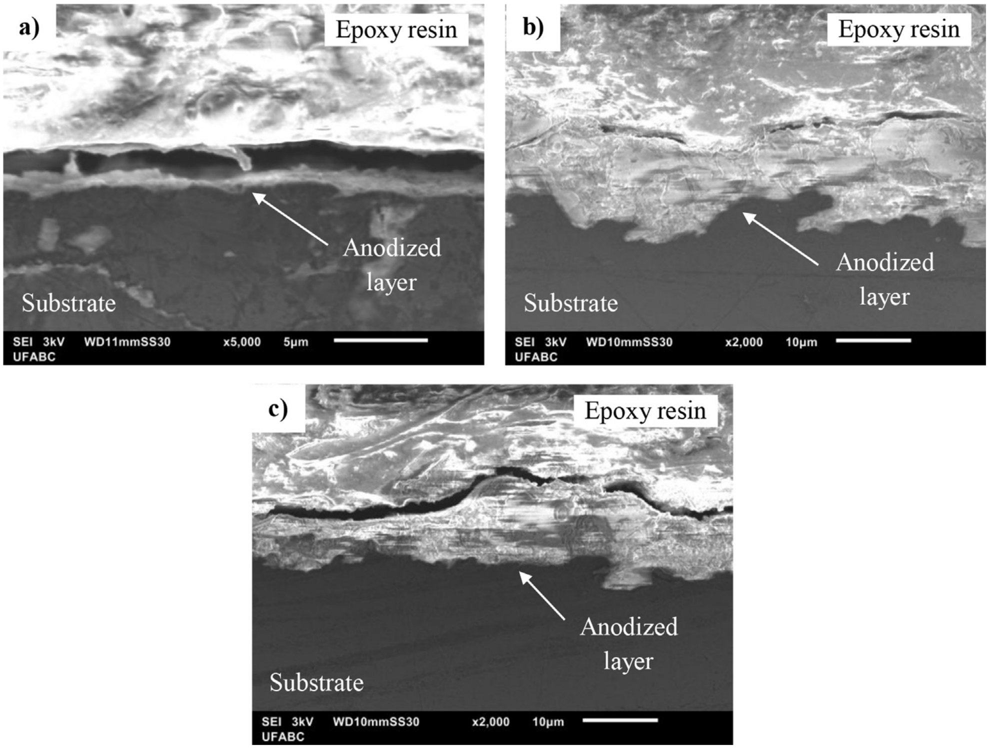

Fig. 3 – SEM images of cross-sections through the anodized layers formed on AZ31B alloy at different current densities: (a) 5, (b) 10, and (c) 20 mA cm^{-2}.

$$2Mg^{2+} + SiO_3^{2-} + 2OH^- \rightarrow Mg_2SiO_4 + H_2O \quad (4)$$

The Si 2p core leves for the anodized samples are shown in Fig. 8, whereas the fitted parameters are displayed in Table 2. The spectrum for the sample anodized at 5 mA cm^{-2} was deconvoluted into two components. The low binding energy one was assigned to silicate species (Mg_2SiO_4) whereas the high binding energy component was due to silica-type bonds (SiO_2) [48,50]. Silica bonds predominate over silicate, as seen in Table 2. The formation of SiO_2 can take place due to the reaction between magnesium ions and silicate anions, according to Eq. (5) [17]:

$$2Mg^{2+} + 2SiO_3^{2-} \rightarrow Mg_2SiO_4 + SiO_2 \quad (5)$$

Conversely, the Si 2p core levels for the samples anodized at 10 mA cm^{-2} and 20 mA cm^{-2} showed one single component which was assigned to silicate-type species. These results point that reaction (4) is favored by increasing the current density of the anodizing process.

Fig. 9 shows the XPS spectra corresponding to the O 1s core levels for the anodized samples. The spectra were deconvoluted into two components, independently of the current density employed during the anodization procedure. Although a third component at approximately 535 eV was also found in all spectra, it corresponds to an Auger peak of sodium (NaKLL), revealing that sodium species are adsorbed on the sample surface during anodization in the mixed NaOH/Na_2SiO_3 electrolyte, in accordance with the results shown in the survey spectra (Fig. 6). The component at the lowest binding energy is assigned to O^{2-} species such as Mg_2SiO_4 whereas the highest binding energy component is assigned to hydroxide species such as $Mg(OH)_2$. These species were also found in the spectra for the Mg 1s core levels, confirming that the anodic layers mainly consisted of a mixture of Mg_2SiO_4 and $Mg(OH)_2$, being SiO_2 also part of the film produced at 5 mA cm^{-2}.

3.3. *Electrochemical characterization*

3.3.1. *Electrochemical impedance spectroscopy (EIS)*

The electrochemical impedance spectra recorded for the as polished and anodized AZ31B alloy materials after 1 h of immersion in PBS at room temperature are shown in the form of Nyquist plots in Fig. 10, whereas the corresponding Bode plots (phase angle vs. frequency and impedance modulus vs. frequency) are displayed in Fig. 11.

The Nyquist plots are characterized by the occurrence of depressed capacitive semicircles at intermediate frequencies, and they showed a larger diameter for the samples subjected to anodization. The diameter of the capacitive loop is associated with the charge transfer resistance, which is related to the corrosion resistance of the electrode material in the test solution [51]. The as polished sample presented the lowest impedance values, indicating the poor protective character of the oxide film naturally formed on its surface. Anodization promoted an increase of the corrosion resistance as denoted by the significantly greater diameter of the impedance loop with respect to that of the as-polished sample. The anodized layer produced at 20 mA cm^{-2} current density showed the

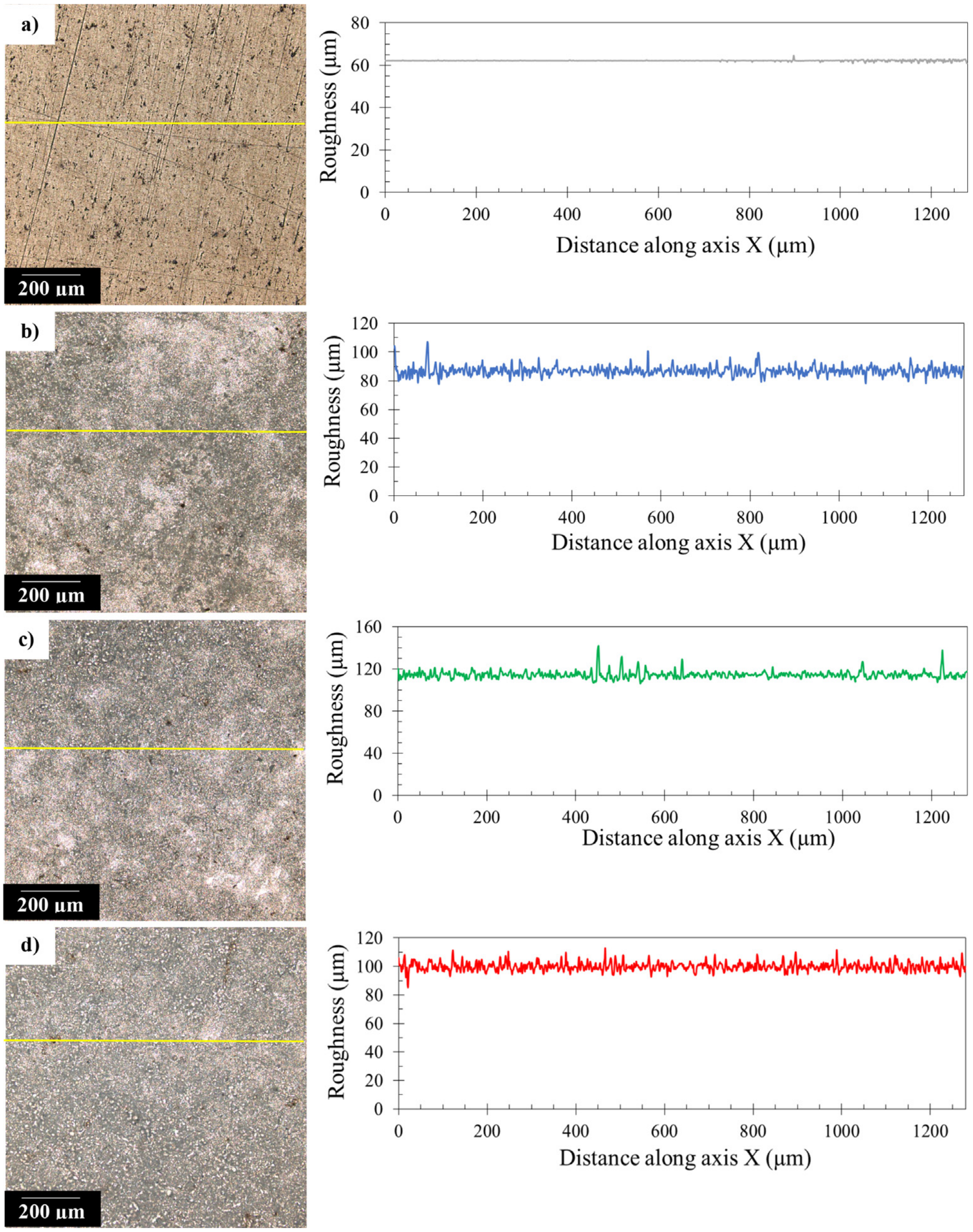

Fig. 4 – 2D images and representative roughness profiles obtained using CLSM for various AZ31B alloy samples: (a) as polished; and after electrochemical anodization imposing constant current density values: (b) 5, (c) 10, and (d) 20 mA cm^{-2}.

highest impedance values, evidencing that it presented the most protective surface against corrosion in PBS.

Inspection of the Bode plots shown in Fig. 11 confirm these observations. The phase angle peak recorded for the anodized samples raised to more capacitive values, ca. −70° than for the as polished sample (approximately −60°), as seen in Fig. 11a. Additionally, the phase angle peaks shifted to lower frequencies, implying in the shift of breakdown frequencies related to the transition from capacitive to resistive regimes (i.e., at which the phase angle amounts −45°) to lower frequencies for the anodized samples, especially for the anodized film obtained at 20 mA cm^{-2}. Therefore, the barrier characteristics of its surface layer are enhanced, indicating its superior corrosion resistance when compared to the other anodized layers and to the as-polished alloy.

Additional evidence for the superior corrosion resistance of the anodized layer produced at 20 mA cm^{-2} film is derived from the log |Z| vs. log frequency plots shown in Fig. 11b.

Table 1 – Average roughness (R_a) values obtained from CLSM imaging for AZ31B alloy samples in the as polished and after electrochemical anodization at the indicated constant current density values.

Sample	Ra (μm)
Polished	0.07 ± 0.01
5 mA.cm^{-2}	2.65 ± 0.24
10 mA.cm^{-2}	2.24 ± 0.31
20 mA.cm^{-2}	2.80 ± 0.21

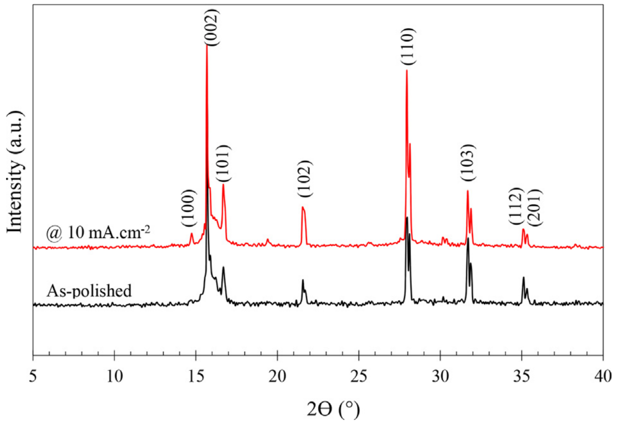

Fig. 5 – XRD patterns of the as polished and 10 mA cm^{-2} samples.

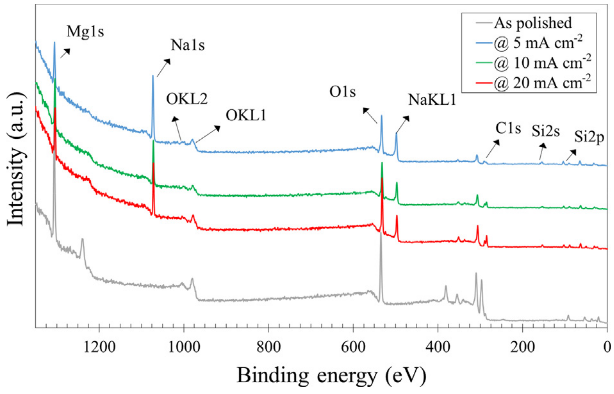

Fig. 6 – XPS survey spectra recorded for various AZ31B alloy samples as indicated in the graph.

Although this system presents only slightly higher impedance values in the low frequency limit than the sample anodized at 10 mA cm^{-2}, the impedance values were 1–2 orders of magnitude bigger than for the material anodized using the lowest current density. The as-polished condition was the least corrosion resistant, as indicated by its low impedance values. Moreover, the capacitive behavior denoted by the linear portion with slope close to −1 at intermediate frequencies was lost at higher frequencies for the as-polished condition (impedance modulus becoming almost independent of the applied frequency at approximately 10 Hz), evidencing its resistance-controlled character. This feature indicates that charge transfer reactions are taking place at the metal/electrolyte interface which is associated with a corroding surface [52,53]. This phenomenon is slowed down for the anodized samples, especially for the layer formed at 20 mA cm^{-2}, confirming its remarkably greater protective ability against electrolyte penetration and the onset of corrosion at the metal/anodized film interface.

The experimental EIS data were fitted using equivalent electrical circuits (EECs) to give a more quantitative interpretation of the data. The EECs shown in Fig. 12 gave the best fitting to the experimental data. Constant phase elements (CPE) were used instead of pure capacitors to account for the heterogeneity of the electrode surface [54]. The impedance of a CPE (Z_{CPE}) is calculated from Eq. (6) where j is the complex operator, ω is the angular frequency, Q is the magnitude of the CPE (related to its capacitance) and n is the exponent of the CPE, being equal to 1 for an ideal capacitor, 0.5 for diffusion-controlled electrodes and n = 0 for an ideal resistor. Intermediate values of n (0 < n < 1) are obtained for actual electrodes [55].

$$Z_{CPE} = \left[Q(j\omega)^{n}\right]^{-1} \tag{6}$$

The EEC in Fig. 12a provided the best fitting to the experimental data obtained for the as-polished sample. The physical meaning of each circuit parameter was considered as follows: R_1 is the electrolyte resistance, CPE_1 and R_2 are the capacitance of the surface oxide film naturally formed in the solution and its corresponding resistance, CPE_2 and R_3 and the double layer capacitance and the charge transfer resistance. The same circuit was adopted by other authors for uncoated magnesium alloys in saline solutions [56,57]. The EEC in Fig. 12b was used to fit the data of the anodized samples. In this case, the first time constant is related to the anodized layer. CPE_1 and R_2 are, therefore, the capacitance and resistance of the anodic film. The other parameters have the same physical meaning as those of the circuit shown in Fig. 12a. The values of the circuit parameters are displayed in Table 3.

The protective character of the anodized layer obtained at 20 mA cm^{-2} can be realized from its high values of R_2 and R_3 when compared to the other anodized samples and the as-polished surface, confirming the qualitative indications described above for the Nyquist and Bode plots. Moreover, there is a clear decreasing trend of the values of both CPE_1 and CPE_2 with increasing the current density of the anodization process. According to the literature [58], the capacitance values of a surface film are related to the effective area exposed to the electrolyte. It is expected that a more compact layer should present lower capacitances than more defective, porous ones. The SEM micrographs shown in Fig. 1 have indicated an increasing compactness of the anodized films with the current density of the anodization process. The decreasing trend of the CPE values in Table 3 for the samples obtained at larger current densities would be related to this morphological feature. Next section gives additional evidence on the porosity of the anodized layers.

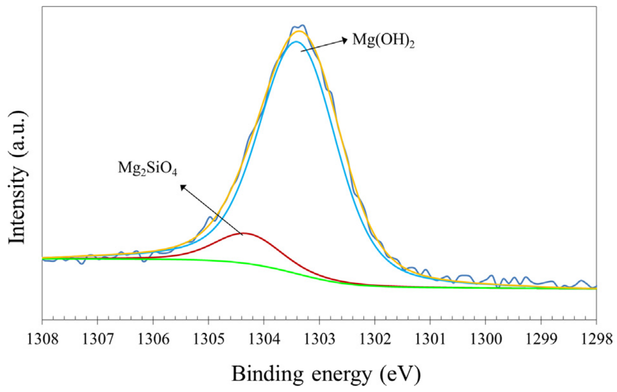

Fig. 7 – XPS spectrum of the Mg1s core level recorded for AZ31B alloy anodized at 20 mA cm^{-2}.

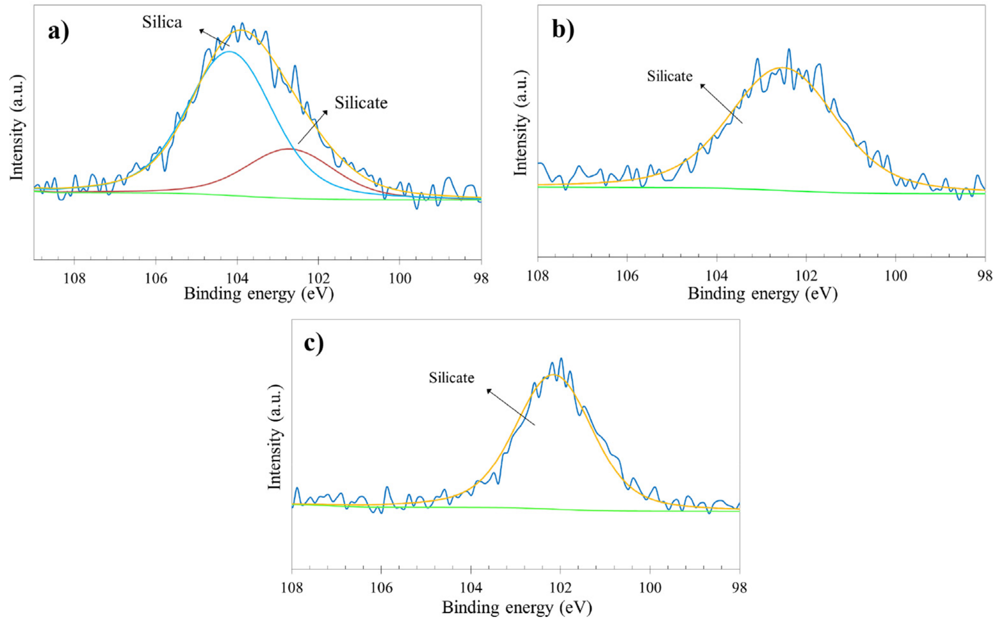

Fig. 8 – XPS spectra of Si2p core levels recorded for AZ31B alloy samples anodized at different current densities: (a) 5, (b) 10, and (c) 20 mA cm^{-2}.

Table 2 – Fitting parameters for the XPS Si2p core levels of anodized AZ31B alloy samples.

Component	@ 5 mA cm^{-2}		@ 10 mA cm^{-2}		@ 20 mA cm^{-2}	
	Silica	Silicate	Silica	Silicate	Silica	Silicate
BE (eV)	104.1	102.6	–	102.4	–	102.0
FWHM (eV)	2.49	2.57	–	2.81	–	2.04
at.%	73.9	26.1	–	100	–	100

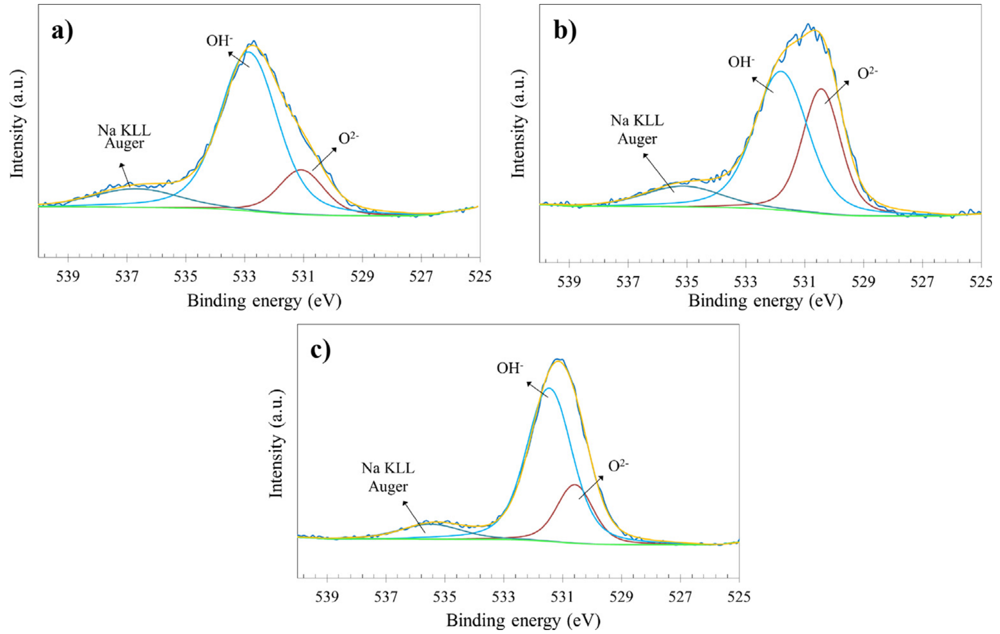

Fig. 9 – XPS spectra of O1s core levels recorded for AZ31B alloy samples anodized at different current densities: (a) 5, (b) 10, and (c) 20 mA cm^{-2}.

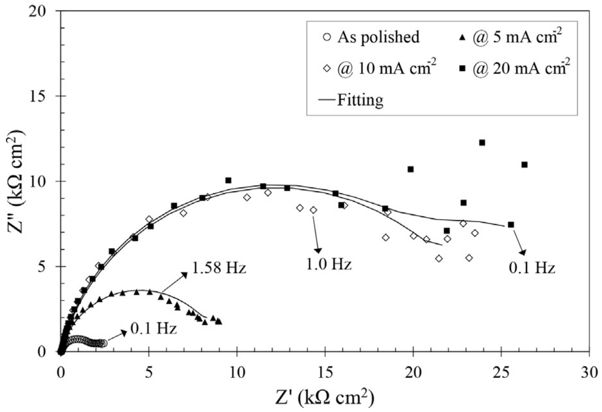

Fig. 10 – Nyquist plots of as polished and anodized AZ31B alloy samples immersed in PBS at room temperature. The spectra were recorded at the OCP value attained by the materials after 30 min.

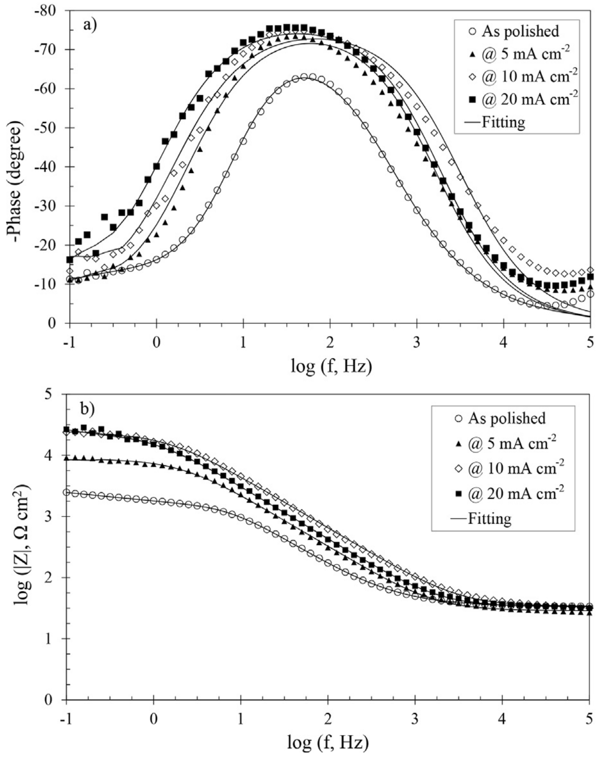

Fig. 11 – Bode plots of the as polished and anodized AZ31B alloy samples immersed in PBS at room temperature. (a) Bode-phase, and (b) Bode-impedance modulus plots.

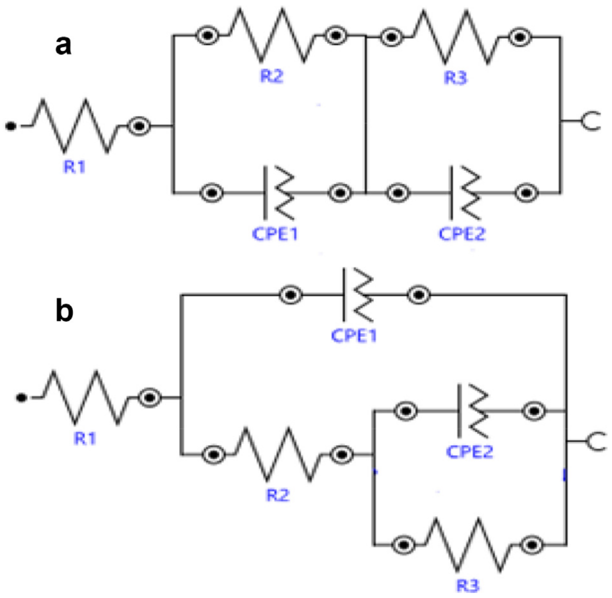

Fig. 12 – Fig. 12. EECs used to fit the experimental EIS data of the: a) as polished and b) anodized AZ31B samples.

3.3.2. *Potentiodynamic polarization curves*

Potentiodynamic polarization curves of the as-polished and anodized samples obtained in PBS at room temperature are shown in Fig. 13. The corrosion current densities (j_{corr}) and corrosion potential (E_{corr}) values were determined from these curves using the Tafel extrapolation method. The procedure could be applied solely to the cathodic branches of the polarization curves as they were under charge transfer control, whereas the onset of passivity affected the shape of the anodic branches in the case of the anodized samples (see the arrow included in Fig. 13). The values of the electrochemical parameters obtained by Tafel analysis are displayed in Table 4.

It was found that the corrosion potential values were not significantly modified by the anodization process. If one notices the standard deviation of the values shown in Table 4, E_{corr} values can be considered to remain almost the same for all the investigated surface conditions. The values of j_{corr}, in turn, markedly decreased due to the anodization treatment. The results indicate that the anodized layers formed on the surface of AZ31B operate as an effective barrier against electrolyte penetration. The j_{corr} values are similar, though, for all the anodized samples, and differences in the electrochemical behavior cannot be distinguished among the treated samples on the basis these parameters. That is, the effect of the anodizing current density on the overall corrosion rate of the coated AZ31B alloy is not clearly observed from these data. It is, therefore, important to examine the anodic branches of the polarization with more detail. It is seen that the anodic current densities of the films obtained at 10 mA cm^{-2} and

Table 3 – Circuit parameters for the EIS data of the as polished and anodized AZ31B samples.

Circuit parameter	As polished	@ 5 mA cm^{-2}	@ 10 mA cm^{-2}	@ 20 mA cm^{-2}
R_1 (Ω cm^2)	42.8	35.3	41.6	41.3
Q_1 (10^{-6} Mho s^n)	21.3	9.66	6.54	5.01
n_1	0.84	0.86	0.85	0.87
R_2 (kΩ cm^2)	2.38	10.8	22.4	29.4
Q_2 (10^{-4} Mho s^n)	8.92	7.99	3.73	1.76
n_2	0.65	0.85	0.91	0.92
R_3 (kΩ cm^2)	0.77	2.35	6.30	9.62

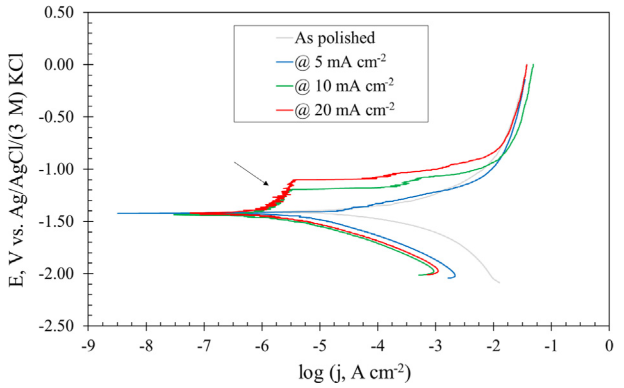

Fig. 13 – Potentiodynamic polarization curves measured for as polished and anodized. AZ31B alloy samples immersed in PBS at room temperature.

20 mA cm^{-2} are significantly lower than those of the as polished sample as the potential is shifted in the positive direction. In addition, a small region where the anodic current density presents a slow increase with the applied potential (a small pseudo-passive behavior) can be clearly seen for these samples which is absent from the curve of the as-polished surface. In this respect, the anodized layer formed on AZ31B by the anodization treatment effectively slowed down the corrosion process of the alloy. The film produced using 20 mA cm^{-2} presented the widest pseudo-passive region and the lowest anodic current densities over the remaining potential range, thus revealing an improvement of their protective ability. These results confirm the observations derived from the analysis of EIS data. Yet, it is noteworthy that the film obtained at 5 mA cm^{-2} presents a more active behavior when compared to the anodized films produced at higher current densities. Moreover, the anodic current densities for this film are the highest among the anodized samples and even than those of the as polished alloy.

The observations regarding the global electrochemical behavior of the anodized AZ31B alloy must be related to the morphological features found in Section 3.1 (in particular with regards to Fig. 1). According to Table 4, the porosity ratios were much smaller for the anodized layers produced at 10 mA cm^{-2} (see Fig. 1c) and at 20 mA cm^{-2} (Fig. 1d), which correlate well with their higher impedance values in the low frequency range (cf. Figs. 10 and 11b), while the widest passive region in the polarization curves was observed for the anodized film produced at the high current density (see Fig. 13). The porosity percentage is commonly associated with a function of the spark potential which, in turn, is a function of the applied current density [59–61]. Furthermore, when the current density rises, small sparks change into larger ones, and it moves faster during the anodization process [26]. Thus, the molten oxide spreads more uniformly over the magnesium surface. This could be a reason for the decrease of the porosity percentage observed for those conditions. Whereas the conductivity to produce the anodized film at 5 mA cm^{-2}, in turn, would be insufficient. This, in turn, leads to a porous coating, and would assist the quicker penetration of aggressive species present in the corrosive medium. The EIS data are in good agreement with this observation, as one can see from the fitted parameters shown in Table 3.

It is also relevant to observe that the surface chemistry of the anodized layers was very similar for all samples, as seen in section 3.2. In this respect, the current density of the anodizing treatment did not affect the chemical state of the species in the anodized layer but deeply influenced its morphology, playing a critical role on its overall corrosion resistance.

3.4. *Localized physicochemical characterization*

The electrochemical behavior of the AZ31B alloy in the as-polished and anodized conditions was further evaluated using scanning electrochemical microscopy (SECM) in order to resolve eventual distributions of electrochemical activity over the exposed sample. The Pt UME was employed to monitor the evolution of hydrogen gas from the corroding AZ31B alloy surface. The potential of the UME was set at 0.0 V vs. Ag/AgCl/(3 M, KCl) to produce the oxidation of hydrogen at the tip according to:

$$H_2 \rightarrow 2H^+ + 2e^- \qquad (7)$$

The AZ31B alloy substrate was left unbiased in order to monitor its spontaneous corrosion behaviour in the electrolyte. Fig. 14 shows representative SECM 2D maps recorded over randomly chosen regions near the center of the samples under investigation. The size of the scanned area was 400 μm × 200 μm, small enough to be scanned by the small Pt tip required for the SECM operation, whereas being big enough to resolve the local corrosion microcells required for the onset of electrochemical corrosion on an unbiased material (i.e, under spontaneous corrosion conditions in the test electrolyte). It must be noticed that the current scales given at the right side of each map are related to the magnitude of the H_2 flux detected by the Pt UME [62]. Accordingly, bigger currents are associated with localized sites generating greater amounts of H_2 at the surface of the AZ31B substrate and, correspondingly, they arise from a more intense corrosion process of the material leading to magnesium dissolution.

Table 4 – Electrochemical parameters obtained from the potentiodynamic polarization curves shown in Fig. 11. The last column lists porosity values (P%) for the surface layers formed on the anodized samples.

Condition	E_{corr} (V vs. Ag/AgCl/(3 M) KCl)	j_{corr} (μA cm^{-2})	R_p (kΩ cm^2)	b_a^{AZ31B} (mV dec^{-1})	P (%)
As polished	−1.407 ± 0.004	30.6 ± 8.4	0.720	100.34	–
@ 5 mA cm^{-2}	−1.464 ± 0.091	3.7 ± 2.9	5.676	–	9.39
@ 10 mA cm^{-2}	−1.455 ± 0.042	1.4 ± 0.6	38.20	–	0.98
@ 20 mA cm^{-2}	−1.473 ± 0.070	2.0 ± 0.8	51.32	–	0.85

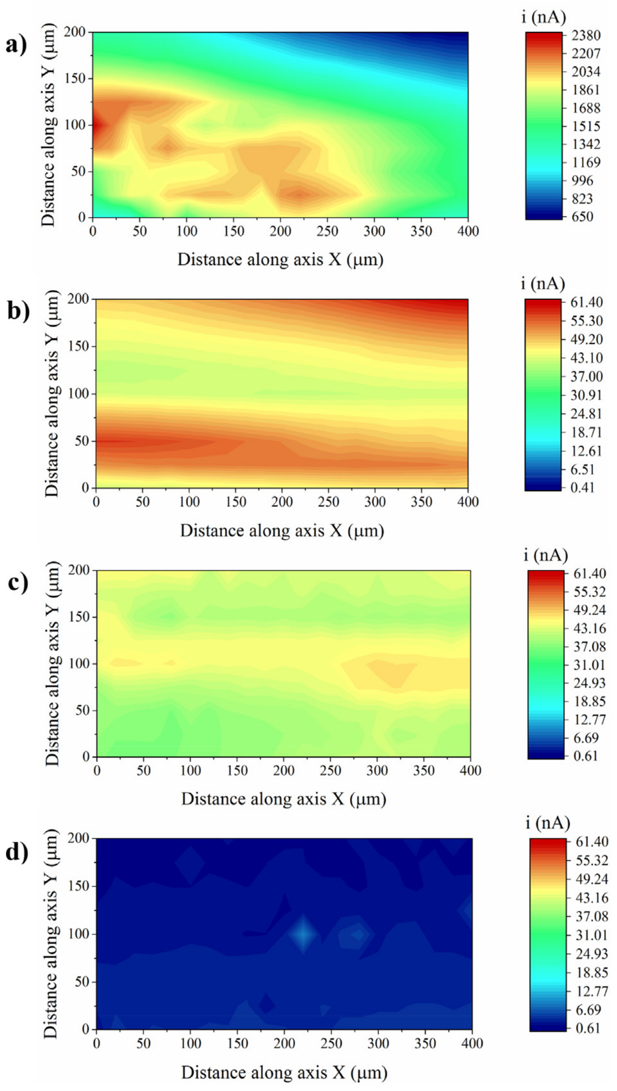

Fig. 14 – SECM 2D maps monitoring H_2 evolution from the surface of AZ31B alloy samples immersed in PBS at room temperature: (a) as polished, and after anodization at different current densities: (b) 5, (c) 10, and (d) 20 mA cm^{-2}. Tip potential: 0.0 V vs. Ag/AgCl/(3 M) KCl; tip-sample distance: 10 μm; substrate potential: unbiased. The tip current scales are the same for all the anodized sample maps, whereas it encompasses bigger currents in the case of the as polished condition (a). Larger currents, e.g. red domains, correspond to higher fluxes of H_2 evolving from the spontaneously corroding substrate.

From a cursory comparison of the SECM maps shown in Fig. 14, it is readily observed that the impact of corrosion processes was much more intense at the surface of the as polished alloy in PBS at room temperature (cf. Fig. 14a), as denoted by the high currents for hydrogen oxidation that were measured at the tip while scanning the probed area. The tip currents were reduced by almost two orders of magnitude after the anodizing treatment. Therefore, the surface modification produced to the AZ31B alloy by electrochemical anodization led to the material exhibiting a major decrease of the local currents monitored by SECM, thus indicating that the access of the aggressive species contained in the test electrolyte to the underlying metallic substrate was effectively reduced. Although complete passivation of the AZ31B surface could not be attained by this treatment, a significant decrease of the corrosion rates could be afforded, which can be regarded of interest when biodegradable implant materials of controlled degradation rates should be envisaged.

Among the anodized samples, the highest tip currents were observed for the sample anodized at 5 mA cm^{-2} when compared to the samples anodized at higher current densities, as observed in Fig. 14b-d. It is well known that SECM is very sensitive to defects in coated surfaces [63], therefore the higher tip currents measured at the samples anodized using the smaller current densities with respect to that produced with the 20 mA cm^{-2} condition, can indicate that the probed areas present more active sites for H_2 evolution as the magnesium substrate corrodes. The spatial resolution of the technique allows to sense these species evolving from small defective sites which can be probed by the UME while scanning the surface treated at 20 mA cm^{-2}. The heterogeneous morphology of the anodized surface can lead to variations of roughness as shown in Section 3.1, whereas the presence of pores and microcracks over the treated surface could not be discarded. As a result, the H_2 fluxes detected by the UME would correlate with those local imperfections, allowing SECM to detect them accurately. Furthermore, these SECM observations on the local electrochemical response of the anodized layers correlate well with the global response characterized using EIS and potentiodynamic polarization in Section 3.3, and they confirm that the sample anodized using 20 mA cm^{-2} current density exhibited the lowest electrochemical activity both in micro- and millimeter scales.

Since previous investigations using SECM have shown that an $Mg(OH)_2$-covered surface on AZ63 magnesium alloy catalytically enhanced hydrogen evolution under anodic polarization [64,65], the smaller electrochemical activity observed in this work for the surface layers produced in mixed $NaOH + Na_2SiO_3$ aqueous solution must correlate with their chemical composition. The XPS data of Section 3.2 showed that greater silicate ratios (and consequently, smaller $Mg(OH)_2$ ratios) were obtained when the alloy was anodized with increasingly higher current densities, with a maximum value for the sample treated using the 20 mA cm^{-2} current density. In this way, a more corrosion resistant surface layer was obtained, effectively reducing the corrosion rate of the material in the naturally-aerated PBS test environment.

Further investigation of the local physicochemical characteristics of the investigated materials was performed using the Scanning Kelvin Probe. SKP measures the Volta potential difference between the working electrode and the probe, which vibrates above the surface sample in air. In this way, the two surfaces form a capacitor, and according to the probe vibration and its local variation, an AC current is generated. The amplitude of this current is directly proportional to the local Volta potential difference, and it is possible to distinguish areas with a more anodic or cathodic character on the investigated surface from their relative Volta potential values. Although these measurements are performed in air (i.e., when the sample is not effectively exposed to an aqueous

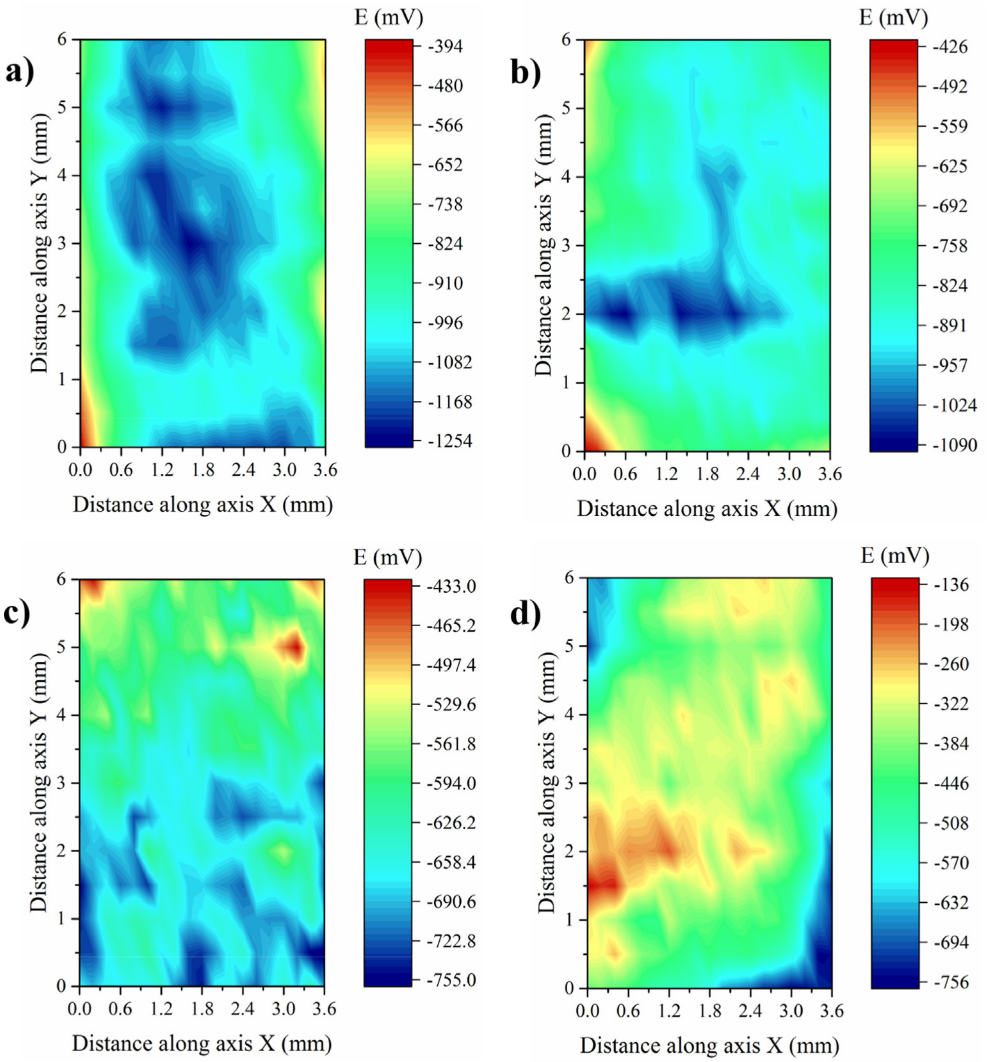

Fig. 15 – SKP surface distributions of AZ31B alloy as polished (a) and after anodization in 1.0 M NaOH + 0.5 M Na_2SiO_3 solution for 5 min at different current densities: (b) 5, (c) 10, and (d) 20 mA cm^{-2}. The anodic regions for each material correspond to the blue domains in the maps.

environment), SKP supplies complementary information for the investigation of local corrosion processes.

2D-maps showing the surface potential distributions obtained over AZ31B alloy samples in the as-polished and in the anodized conditions are presented in Fig. 15. Since the surface Volta potential is related to the changes in electronic energy and the work function, a higher potential value is then associated to an increased work function, and greater energy would be required to remove an electron through the surface region [42]. The naturally formed oxide in the as-polished condition (see Fig. 15a) presented the largest potential difference between cathodic and anodic regions over the surface (namely in excess of 860 mV), attaining a very negative potential in the center of the map. This distinguishable potential variation should act as a driving force for corrosion [66]. On the other hand, the samples with the anodized layers showed less extended areas presenting the more negative potential values, and exhibited smaller potential differences over their surface films. Although this trend was still rather small for the sample anodized at 5 mA cm^{-2}, the two samples obtained applying higher current densities presented both a smaller potential variation between anodic and cathodic areas, and more positive potential values. Among them, the anodized film formed at 20 mA cm^{-2} showed the noblest and less heterogeneous Volta potential distribution by comparison to the other systems, with a similar trend to that evidenced by SECM for the AZ31B samples subjected to anodization (cf. Fig. 14d). In summary, it was found that the Volta potential distributions shown in Fig. 15 correlate well with the surface morphologies observed *ex situ* us methods (see Fig. 1) and with the distributed electrochemical activities monitored *in situ* by SECM (cf. Fig. 14).

3.5. *In vitro* biocompatibility

The *in vitro* biocompatibility of the AZ31B alloy in the as-polished and anodized conditions was evaluated by cytotoxicity tests, taking into account the MTS metabolic activity

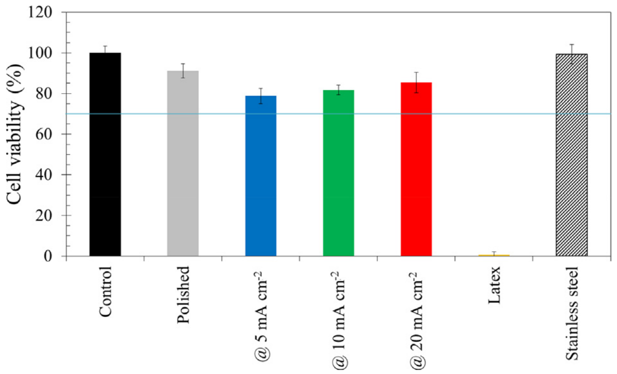

Fig. 16 – Cell viability values determined by the Methyl Tetrazolium (MTS) assay on control (i.e., latex and stainless steel) and AZ31B alloy samples, as polished and after galvanostatic anodization at the indicated current values for 5 min in 1.0 M NaOH + 0.5 M Na_2SiO_3 solution.

assay. The cell viability results are summarized in Fig. 16. According to ISO 10993-5 [67], the cell viability must be below 70% for a material to be considered cytotoxic. Therefore, only the positive control (latex) was cytotoxic, whereas all the anodized samples were not cytotoxic. The highest cell viability was observed for the 20 mA cm^{-2} anodization condition. It is possible to infer that this surface modification treatment provided the best mean to control the anodic dissolution rate of the AZ31B alloy without sacrificing its intrinsic biocompatibility.

4. Discussion

The corrosion mechanism of the anodized samples can be discussed based on the firmly established dependence of the protective ability of anodic films on the synergistic action of thickness, chemical composition and compactness [26,68]. Thickness increase may enhance the barrier properties of the coating, provided it remains compact and with few defects [69]. Compactness is of prime importance for the coating performance against corrosion and it can be triggered by the phases/compounds that constitute the anodic film [69].

Some remarks can be drawn from the previous sections in order to understand the role of the current density of the anodization process on the corrosion mechanism of the anodic films. Firstly, an obvious increase of the coating thickness took place when the current density was raised from 5 to 10 mA cm^{-2} while it was not significantly changed when the current density was further raised to 20 mA cm^{-2} (Fig. 3). Secondly, silicate-type bonds were favored by increasing the current density. While the 5 mA cm^{-2} film was comprised of a mixture of silica and silicate bonds, only silicate bonds were part of the Si2p region of the samples obtained at 10 mA cm^{-2} and 20 mA cm^{-2} (Fig. 8). In the Mg 1s region the XPS spectra of all anodized samples was comprised of a mixture of $Mg(OH)_2$ and Mg_2SiO_4, as described in section 3.2 (Fig. 7). Quantitative analysis of the fitting results referred to the Mg 1s core levels of the anodized samples is shown in Table 5. The relative concentration of Mg_2SiO_4 was greatly enhanced when the current density of the anodization process was increased from 5 to 10 mA cm^{-2}, but was not significantly affected by further increasing the current density to 20 mA cm^{-2}.

One additional and remarkable aspect was related to coating compactness. As shown in Section 3.3, EIS results (EEC parameters displayed in Table 3) and the porosity levels (Table 4) point to the formation of more compact anodic layers as the higher current density increased. In fact, the most compact film was obtained at 20 mA cm^{-2}. Yet, from Section 3.3, the corrosion resistance of the anodized samples was increased in the following order: @ 5 mA cm^{-2} < @ 10 mA cm^{-2} < @ 20 mA cm^{-2}. Furthermore, local currents shown in 2D SECM maps (Fig. 14) and Volta potential distributions (Fig. 15) confirmed the lower electrochemical activity at the surface of the @ 20 mA cm^{-2} sample.

The remarks outlined above allow one to make important observations. Thickness increase was beneficial to the corrosion resistance of the anodic layers. However, it was not the only factor responsible for reducing the corrosion rate, as the thicknesses of the anodic layers obtained at 10 mA cm^{-2} and 20 mA cm^{-2} were similar, but their electrochemical activities were different, as shown in Section 3.4. In the same way, the chemical composition of the anodic films should not be ruled out. According to the literature, Mg_2SiO_4 favors the corrosion resistance of anodic films formed on magnesium alloys by enhancing adhesion between the oxide layer and the substrate due to the shrinking effect of molar volume changes in the film [70,71]. The larger Mg_2SiO_4 concentration in the films formed at 10 mA cm^{-2} and 20 mA cm^{-2} (Table 5) would, therefore, be related to their superior corrosion protection ability when compared to the @ 5 mA cm^{-2} sample. Nonetheless, the chemical similarity between the anodic layers of the @ 10 mA cm^{-2} and @ 20 mA cm^{-2} samples suggest that one further aspect should be related to the lower electrochemical activity of the later.

In fact, as an inevitable part of the anodic film, pores participate in the corrosion mechanism of the anodized samples. As proposed by Song and Shi [20], when an anodized magnesium electrode is immersed in a saline solution, chloride ions reach the substrate by diffusing through pores, dissolving the material at the interface Mg/anodic film. The solution inside the pores becomes saturated with corrosion products (such as $Mg(OH)_2$) and the corrosion process

Table 5 – Relative concentrations of the magnesium compounds obtained by deconvolution of the Mg 1s core levels of anodized AZ31B alloy samples.

Component	@ 5 mA cm^{-2}		@ 10 mA cm^{-2}		@ 20 mA cm^{-2}	
	$Mg(OH)_2$	Mg_2SiO_4	$Mg(OH)_2$	Mg_2SiO_4	$Mg(OH)_2$	Mg_2SiO_4
Relative concentration (%)	91.3	8.7	71.6	28.4	73.9	26.1

proceeds as a reaction between magnesium and $Mg(OH_2)$ saturated NaCl electrolyte. By restricting the porosity level upon the formation of a denser anodic film, the corrosion process is expected to be slowed down, decreasing the corrosion rate. The more compact morphology of the @ 20 mA cm^{-2} sample was qualitatively showed in Fig. 1 and quantitatively assessed by the calculations made in Section 3.3.2. The beneficial effect of increasing current density on the corrosion resistance of anodized layers formed on magnesium alloy is considered to be due to a good balance between new film formation and old film destruction during film growth in the anodization process [26]. The optimum current density level is to be empirically determined. In the present work, the current density of 20 mA cm^{-2} provided the best corrosion resistance. Although the anodic layer obtained at this current level was not impervious to electrolyte penetration and alloy dissolution, as indicated by the potentiodynamic polarization curves (Fig. 13), it allowed to control the corrosion rate of the AZ31B alloy and did not impart any cytotoxic response (Fig. 16) that are attractive issues for biomedical purposes.

5. Conclusions

The surface morphology of the anodized layers was affected by the current density. The most compact layer was obtained at 20 mA cm^{-2}. The anodized films were mainly comprised of a mixture of Mg_2SiO_4 and $Mg(OH)_2$. This composition was little affected by the current density of the anodizing process.

The global electrochemical behavior of the AZ31B alloy was greatly affected by the surface layers produced by electrochemical anodization. The highest corrosion resistance was obtained for the most compact surface layer produced at 20 mA cm^{-2}. SECM was effective at probing the evolution of molecular H_2 from the naturally corroding samples immersed in PBS, as well as to monitor the wide changes in electrochemical reactivity between the investigated surface finishes for AZ31B. The greater corrosion susceptibility of the as-polished material compared to the modified samples by electrochemical anodization was confirmed using SKP mapping. Wider Volta potential distributions accompanied by more negative potential values were found for the as-polished material, and they could be effectively shifted to more positive (i.e., nobler) potentials after the anodization procedures. SKP confirmed the best protective character against localized corrosion of the film anodized at 20 mA cm^{-2}.

The results described here reveal that the current density is a relevant parameter to control the overall corrosion resistance of the AZ31B alloy, and must be characterized in both macroscopic and microscopic scales as to account for local distributions of chemical reactivity in the surface-modified material.

Declaration of Competing Interest

The authors declare that they have no known competing financial interests or personal relationships that could have appeared to influence the work reported in this paper.

Acknowledgements

The authors thank the Brazilian agencies FAPESP (Proc. 2015/22921-6) and CAPES (Finance code 001) for the financial support, and the Multiuser Experimental Facilities (UFABC) for the experimental support for this work.

REFERENCES

[1] Staiger MP, Pietak AM, Huadmai J, Dias G. Magnesium and its alloys as orthopedic biomaterials: a review. Biomaterials 2006;27:1728–34. https://doi.org/10.1016/j.biomaterials.2005.10.003.

[2] Zeng R, Dietzel W, Witte F, Hort N, Blawert C. Progress and challenge for magnesium alloys as biomaterials. Adv Eng Mater 2008;10:3–14. https://doi.org/10.1002/adem.200800035.

[3] Song G. Control of biodegradation of biocompatable magnesium alloys. Corrosion Sci 2007;49:1696–701. https://doi.org/10.1016/j.corsci.2007.01.001.

[4] Zhao D, Witte F, Lu F, Wang J, Li J, Qin L. Current status on clinical applications of magnesium-based orthopaedic implants: a review from clinical translational perspective. Biomaterials 2017;112:287–302. https://doi.org/10.1016/j.biomaterials.2016.10.017.

[5] Witte F. The history of biodegradable magnesium implants: a review. Acta Biomater 2010;6:1680–92. https://doi.org/10.1016/j.actbio.2010.02.028.

[6] Feyerabend F, Wendel H-P, Mihailova B, Heidrich S, Agha NA, Bismayer U, et al. Blood compatibility of magnesium and its alloys. Acta Biomater 2015;25:384–94. https://doi.org/10.1016/j.actbio.2015.07.029.

[7] Li X, Liu X, Wu S, Yeung KWK, Zheng Y, Chu PK. Design of magnesium alloys with controllable degradation for biomedical implants: from bulk to surface. Acta Biomater 2016;45:2–30. https://doi.org/10.1016/j.actbio.2016.09.005.

[8] Agarwal S, Curtin J, Duffy B, Jaiswal S. Biodegradable magnesium alloys for orthopaedic applications: a review on corrosion, biocompatibility and surface modifications. Mater Sci Eng C 2016;68:948–63. https://doi.org/10.1016/j.msec.2016.06.020.

[9] Witte F, Fischer J, Nellesen J, Vogt C, Vogt J, Donath T, et al. In vivo corrosion and corrosion protection of magnesium alloy LAE442. Acta Biomater 2010;6:1792–9. https://doi.org/10.1016/j.actbio.2009.10.012.

[10] Witte F, Kaese V, Haferkamp H, Switzer E, Meyer-Lindenberg A, Wirth CJ, et al. In vivo corrosion of four magnesium alloys and the associated bone response. Biomaterials 2005;26:3557–63. https://doi.org/10.1016/j.biomaterials.2004.09.049.

[11] Kuhlmann J, Bartsch I, Willbold E, Schuchardt S, Holz O, Hort N, et al. Fast escape of hydrogen from gas cavities around corroding magnesium implants. Acta Biomater 2013;9:8714–21. https://doi.org/10.1016/j.actbio.2012.10.008.

[12] Kirkland NT, Birbilis N, Staiger MP. Assessing the corrosion of biodegradable magnesium implants: a critical review of current methodologies and their limitations. Acta Mater 2012;8:925–36. https://doi.org/10.1016/j.actbio.2011.11.014.

[13] Wan P, Tan L, Yang K. Surface modification on biodegradable magnesium alloys as orthopedic implant materials to improve the bio-adaptability: a review. J Mater Sci Technol 2016;32:827–34. https://doi.org/10.1016/j.jmst.2016.05.003.

[14] Tan L, Yu X, Wan P, Yang K. Biodegradable materials for bone repairs: a review. J Mater Sci Technol 2013;29:503–13. https://doi.org/10.1016/j.jmst.2013.03.002.

[15] Tan L, Wang Q, Lin X, Wan P, Zhang G, Zhang Q, et al. Loss of mechanical properties in vivo and bone-implant interface strength of AZ31B magnesium alloy screws with Si-containing coating. Acta Biomater 2014;10:2333–40. https://doi.org/10.1016/j.actbio.2013.12.020.

[16] Pogorielov M, Husak E, Solodivnik A, Zhdanov S. Magnesium-based biodegradable alloys: degradation, application, and alloying elements. Interv Med Appl Sci 2017;9:27–38. https://doi.org/10.1556/1646.9.2017.04.

[17] Hornberger H, Virtanen S, Boccaccini AR. Biomedical coatings on magnesium alloys - a review. Acta Biomater 2012;8:2442–55. https://doi.org/10.1016/j.actbio.2012.04.012.

[18] Fukuda H, Matsumoto Y. Effects of Na_2SiO_3 on anodization of Mg-Al-Zn alloy in 3 M KOH solution. Corrosion Sci 2004;46:2135–42. https://doi.org/10.1016/j.corsci.2004.02.001.

[19] Santamaria M, Di Quarto F, Zanna S, Marcus P. The influence of surface treatment on the anodizing of magnesium in alkaline solution. Electrochim Acta 2011;56:10533–42. https://doi.org/10.1016/j.electacta.2011.05.027.

[20] Song GL, Shi Z. Corrosion mechanism and evaluation of anodized magnesium alloys. Corrosion Sci 2014;85:126–40. https://doi.org/10.1016/j.corsci.2014.04.008.

[21] Blawert C, Dietzel W, Ghali E, Song G. Anodizing treatments for magnesium alloys and their effect on corrosion resistance in various environments. Adv Eng Mater 2006;8:511–33. https://doi.org/10.1002/adem.200500257.

[22] Hiromoto S, Yamamoto A. Control of degradation rate of bioabsorbable magnesium by anodization and steam treatment. Mater Sci Eng C 2010;30:1085–93. https://doi.org/10.1016/j.msec.2010.06.001.

[23] Xue D, Yun Y, Schulz MJ, Shanov V. Corrosion protection of biodegradable magnesium implants using anodization. Mater Sci Eng C 2011;31:215–23. https://doi.org/10.1016/j.msec.2010.08.019.

[24] Zhang RF, Shan DY, Chen RS, Han EH. Effects of electric parameters on properties of anodic coatings formed on magnesium alloys. Mater Chem Phys 2008;107:356–63. https://doi.org/10.1016/j.matchemphys.2007.07.027.

[25] Ximei W, Liqun Z, Huicong L, Weiping L. Influence of surface pretreatment on the anodizing film of Mg alloy and the mechanism of the ultrasound during the pretreatment. Surf Coating Technol 2008;202:4210–7. https://doi.org/10.1016/j.surfcoat.2008.03.018.

[26] Chai L, Yu X, Yang Z, Wang Y, Okido M. Anodizing of magnesium alloy AZ31 in alkaline solutions with silicate under continuous sparking. Corrosion Sci 2008;50:3274–9. https://doi.org/10.1016/j.corsci.2008.08.038.

[27] Ezhilselvi V, Nithin J, Balaraju JN, Subramanian S. The influence of current density on the morphology and corrosion properties of MAO coatings on AZ31B magnesium alloy. Surf Coating Technol 2016;288:221–9. https://doi.org/10.1016/j.surfcoat.2016.01.040.

[28] Yabuki A, Sakai M. Anodic films formed on magnesium in organic, silicate-containing electrolytes. Corrosion Sci 2009;51:793–8. https://doi.org/10.1016/j.corsci.2009.02.001.

[29] Zhu L, Li Y, Li W. Influence of silica sol particle behavior on the magnesium anodizing process with different anions addition. Surf Coating Technol 2008;202:5853–7. https://doi.org/10.1016/j.surfcoat.2008.06.157.

[30] Pak SN, Jiang Z, Yao Z, Ju JM, Ju KS, Pak UJ. Fabrication of environmentally friendly anti-corrosive composite coatings on AZ31B Mg alloy by plasma electrolytic oxidation and phytic acid/3-aminopropyltrimethoxysilane post treatment. Surf Coating Technol 2017;325:579–87. https://doi.org/10.1016/j.surfcoat.2017.07.003.

[31] da Silva RMP, Milagre MX, de Oliveira LA, Donatus U, Antunes RA, Costa I. The local electrochemical behavior of the AA2098-T351 and surface preparation effects investigated by scanning electrochemical microscopy. Surf Interface Anal 2019;51:982–92. https://doi.org/10.1002/sia.6682.

[32] Zhou H-R, Li X-G, Dong C-F, Xiao K, Li T. Corrosion behavior of aluminum alloys in Na_2SO_4 solution using the scanning electrochemical microscopy technique. Int J Miner Metall Mater 2009;16:84–8. https://doi.org/10.1016/S1674-4799(09)60014-5.

[33] Wang S, Peng H, Shao Z, Zhao Q, Du N. Sealing of anodized aluminum with phytic acid solution. Surf Coating Technol 2016;286:155–64. https://doi.org/10.1016/j.surfcoat.2015.12.024.

[34] González S, Santana JJ, González-García Y, Fernández-Mérida L, Souto RM. Scanning electrochemical microscopy for the investigation of localized degradation processes in coated metals: effect of oxygen. Corrosion Sci 2011;53:1910–5. https://doi.org/10.1016/j.corsci.2011.02.008.

[35] de Oliveira MCL, Correa OV, da Silva RMP, de Lima NB, de Oliveira JTD, de Oliveira LA. Structural, Adhesion and electrochemical characterization of electroless plated Ni-P-carbon black composite films on API 5L X80 steel. J Mater Eng Perform 2019;28:4751–81. https://doi.org/10.1007/s11665-019-04245-2.

[36] Sun M, Xiao K, Dong C, Li X, Zhong P. Electrochemical and initial corrosion behavior of ultrahigh strength steel by scanning Kelvin probe. J Mater Eng Perform 2013;22:815–22. https://doi.org/10.1007/s11665-012-0335-8.

[37] Izquierdo J, Fernández-Pérez BM, Filotás D, Őri Z, Kiss A, Martín-Gómez RT, et al. Imaging of concentration distributions and hydrogen evolution on corroding magnesium exposed to aqueous environments using scanning electrochemical microscopy. Electroanalysis 2016;28:2354–66. https://doi.org/10.1002/elan.201600265.

[38] Thomas S, Gharbi O, Salleh SH, Volovitch P, Ogle K, Birbilis N. On the effect of Fe concentration on Mg dissolution and activation studied using atomic emission spectroelectrochemistry and scanning electrochemical microscopy. Electrochim Acta 2016;210:271–84. https://doi.org/10.1016/j.electacta.2016.05.164.

[39] Jamali SS, Moulton SE, Tallman DE, Zhao Y, Weber J, Wallace GG. Self-healing characteristic of praseodymium conversion coating on AZNd Mg alloy studied by scanning electrochemical microscopy. Electrochem Commun 2017;76:6–9. https://doi.org/10.1016/j.elecom.2017.01.004.

[40] Mena-Morcillo E, Veleva LP, Wipf DO. Multi-scale monitoring the first stages of electrochemical behavior of AZ31B magnesium alloy in simulated body fluid. J Electrochem Soc 2018;165:C749–55. https://doi.org/10.1149/2.0291811jes.

[41] de Oliveira LA, da Silva RMP, Antunes RA. Scanning electrochemical microscopy (SECM) study of the electrochemical behavior of anodized AZ31B magnesium alloy in simulated body fluid. Mater Res 2019;22:e20190079. https://doi.org/10.1590/1980-5373-MR-2019-0079.

[42] Wang Y, Wang J, Zhang J, Zhang Z. Effects of spark discharge on the anodic coatings on magnesium alloy. Mater Lett 2006;60:474–8. https://doi.org/10.1016/j.matlet.2005.09.015.

[43] Chenglong L, Dazhi Y, Guoqiang L, Min Q. Corrosion resistance and hemocompatibility of multilayered Ti/TiN-coated surgical AISI 316L stainless steel. Mater Lett 2005;59:3813–9. https://doi.org/10.1016/j.matlet.2005.06.058.

[44] de Oliveira MCL, Pereira VSM, Correa OV, Antunes RA. Corrosion performance of anodized AZ91D magnesium alloy: effect of the anodizing potential on the film structure and corrosion behavior. J Mater Eng Perform 2014;23:593–603. https://doi.org/10.1007/s11665-013-0755-0.

[45] Pardo A, Merino MC, Coy AE, Arrabal R, Viejo F, Matykina E. Corrosion behaviour of magnesium/aluminium alloys in 3.5

wt.% NaCl. Corrosion Sci 2008;50:823–34. https://doi.org/10.1016/j.corsci.2007.11.005.

[46] El Mahallawy NA, Shoeib MA, Abouelenain MH. AZ91 magnesium alloys: anodizing of using environmental friendly electrolytes. J Surf Eng Mater Adv Technol 2011;1:62–72. https://doi.org/10.4236/jsemat.2011.12010.

[47] Man C, Dong C, Fang Y, Xiao K, Guo C, He G, et al. The Corrosion behavior of magnesium alloy AZ31 in hot and dry atmospheric environment in Turpan, China. Int J Electrochem Sci 2015;10:8691–705.

[48] Wang Q, Tan L, Yang K. Preparation and in vitro degradation characterization of Si-containing coating on AZ31B alloy. Mater Technol 2016;31:828–35. https://doi.org/10.1080/10667857.2016.1254402.

[49] Darband GB, Aliofkhazraei M, Hamghalam P, Valizade N. Plasma electrolytic oxidation of magnesium and its alloys: mechanism, properties and applications. J Magnes Alloy 2017;5:74–132. https://doi.org/10.1016/j.jma.2017.02.004.

[50] Li ZJ, Yuan Y, Jing XY. Comparison of plasma electrolytic oxidation coatings on Mg – Li alloy formed in molybdate/silicate and aluminate/silicate composite electrolytes. Mater Corros 2014;65:493–501. https://doi.org/10.1002/maco.201206652.

[51] Fernández-Pérez BM, González-Guzmán JA, González S, Souto RM. Electrochemical impedance spectroscopy investigation of the corrosion resistance of a waterborne acrylic coating containing active electrochemical pigments for the protection of carbon steel. Int J Electrochem Sci 2014;9:2067–79.

[52] Say WC, Chen CC, Hsieh SJ. Electrochemical characterization of non-chromate surface treatments on AZ80 magnesium. Mater Char 2008;59:1400–6. https://doi.org/10.1016/j.matchar.2007.12.007.

[53] Babaei M, Dehghanian C, Vanaki M. Effect of additive on electrochemical corrosion properties of plasma electrolytic oxidation coatings formed on CP Ti under different processing frequency. Appl Surf Sci 2015;357A:712–20. https://doi.org/10.1016/j.apsusc.2015.09.059.

[54] Zhang LJ, Fan JJ, Zhang Z, Cao FH, Zhang JQ, Cao CN. Study on the anodic film formation process of AZ91D magnesium alloy. Electrochim Acta 2007;52:5325–33. https://doi.org/10.1016/j.electacta.2006.12.083.

[55] Ogunsanya IG, Hansson CM. The semiconductor properties of passive films and corrosion behavior of stainless steel reinforcing bars in simulated concrete pore solution. Materialia 2019;6:100321-1–100321-14. https://doi.org/10.1016/j.mtla.2019.100321.

[56] Badawy WA, Hilal NH, El-Rabiee M, Nady H. Electrochemical behavior of Mg and some Mg alloys in aqueous solutions of different pH. Electrochim Acta 2010;55:1880–97. https://doi.org/10.1016/j.electacta.2009.10.083.

[57] Jamesh MI, Wu G, Zhao Y, McKenzie DR, Bilek MMM, Chu PK. Electrochemical corrosion behavior of biodegradable Mg-Y-RE and Mg-Zn-Zr alloys in Ringer's solution and simulated body fluid. Corrosion Sci 2015;91:160–84. https://doi.org/10.1016/j.corsci.2014.11.015.

[58] Santamaria M, Tranchida G, Di Franco F. Corrosion resistance of passive films on different stainless steel grades in food and beverage industry. Corrosion Sci 2020;173:108778-1–108778-12. https://doi.org/10.1016/j.corsci.2020.108778.

[59] Duan H, Du K, Yan C, Wang F. Electrochemical corrosion behavior of composite coatings of sealed MAO film on magnesium alloy AZ91D. Electrochim Acta 2006;51:2898–908. https://doi.org/10.1016/j.electacta.2005.08.026.

[60] Joni MS, Fattah-Alhosseini A. Effect of KOH concentration on the electrochemical behavior of coatings formed by pulsed DC micro-arc oxidation (MAO) on AZ31B Mg alloy. J Alloys Compd 2016;661:237–44. https://doi.org/10.1016/j.jallcom.2015.11.169.

[61] Xinghua G, Maozhong A, Peixia Y, Haixian L, Caina S. Effects of benzotriazole on anodized film formed on AZ31B magnesium alloy in environmental-friendly electrolyte. J Alloys Compd 2009;482:487–97. 101016/jjallcom200904053.

[62] Thomas S, Izquierdo J, Birbilis N, Souto RM. Possibilities and limitations of scanning electrochemical microscopy of Mg and Mg alloys. Corrosion 2015;71:171–83. https://doi.org/10.5006/1483.

[63] Tefashe UM, Dauphin-ducharme P, Danaie M, Cano ZP, Kish JR, Botton GA, et al. Localized corrosion behavior of AZ31B magnesium alloy with an electrodeposited poly (3,4-ethylenedioxythiophene) coating. J Electrochem Soc 2015;162:C536–44. https://doi.org/10.1149/2.0601510jes.

[64] Salleh SH, Thomas S, Yuwono JA, Venkatesan K, Birbilis N. Enhanced hydrogen evolution on Mg $(OH)_2$ covered Mg surfaces. Electrochim Acta 2015;161:144–52. https://doi.org/10.1016/j.electacta.2015.02.079.

[65] Filotás D, Fernández-Pérez BM, Nagy L, Nagy G, Souto RM. A novel scanning electrochemical microscopy strategy for the investigation of anomalous hydrogen evolution from AZ63 magnesium alloy. Sensor Actuator B Chem 2020;308:127691. https://doi.org/10.1016/j.snb.2020.127691.

[66] Talha M, Ma Y, Lin Y, Singh A, Liu W, Kong X. Corrosion behaviour of austenitic stainless steels in phosphate buffer saline solution: synergistic effects of protein concentration, time and nitrogen. New J Chem 2019;43:1943–55. https://doi.org/10.1039/C8NJ04670K.

[67] ISO. Document 10993-5, biological evaluation of medical devices, tests for cytotoxicity: in vitro methods, Part 5, vol. 99. Geneva, Switzerland: International Organization for Standardization; 2009.

[68] Liang J, Srinivasan PB, Blawert C, Dietzel W. Comparison of electrochemical corrosion behaviour of MgO and ZrO_2 coatings on AM50 magnesium alloy formed by plasma electrolytic oxidation. Corrosion Sci 2009;51:2483–92. https://doi.org/10.1016/j.corsci.2009.06.034.

[69] Zhang RF, Zhang SF, Xiang JH, Zhang LH, Zhang YQ, Guo SB. Influence of sodium silicate concentration on properties of micro arc oxidation coatings formed on AZ91HP magnesium alloys. Surf Coating Technol 2012;206:5072–9. https://doi.org/10.1016/j.surfcoat.2012.06.018.

[70] Wang Y, Chen M, Zhao Y. Preparation and corrosion resistance of microarc oxidation-coated biomedical Mg-Zn-Ca alloy in the silicon-phosphorus-mixed electrolyte. ACS Omega 2019;4:20937–47. https://doi.org/10.1021/acsomega.9b01998.

[71] Wu HL, Cheng YL, Li LL, Chen ZH, Wang HM, Zhang Z. The anodization of ZK60 magnesium alloy in alkaline solution containing silicate and the corrosion properties of the anodized films. Appl Surf Sci 2007;253:9387–94. https://doi.org/10.1016/j.apsusc.2007.05.085.